Nucl. Phys. A 1055 (2025) 123005

Contents lists available at ScienceDirect

Nuclear Physics A

journal homepage: www.elsevier.com/locate/nuclphysa

Probing the contribution of various mass fragments in the production of magnetic field during heavy ion collisions

Dhanpat Sharma, Suneel Kumar *

Department of Physics and Astrophysics, Central University of Haryana, Mahendergarh, 123031, India

A R T I C L E I N F O

Keywords:
Magnetic field
Multifragmentation
Rapidity
IQMD
MSTP

A B S T R A C T

This research work delves into the contribution of different mass fragments in the generation of magnetic field during heavy ion collisions (HICs) in the intermediate energy regime. Isospin dependent quantum molecular dynamics (IQMD) framework has been employed as a primary tool for phase space along with minimum spanning tree with momentum cut (MSTP) algorithm for the clusterization process. In this study, temporal evolution of magnetic field due to various mass fragments and its correlation with the impact parameter have been visualized. Moreover, the influence of some significant observables, such as rapidity and transverse momentum on the production of magnetic field due to various mass fragments have been investigated to gain more insights.

1. Introduction

The production of electromagnetic field during heavy ion collisions (HICs) is a fascinating as well as intriguing topic in the contemporary nuclear research [1–4]. Two highly energetic colliding ions generate very powerful magnetic field intensity ($eB \approx 10m_\pi^2$) which has the potential to elicit very interesting transport phenomena such as Chiral Magnetic Effect (CME) [5–9], Chiral Separation Effect (CSE) [10], Chiral Vortical Effect (CVE) [6,11], Chiral Electric Separation Effect (CESE), Chiral Magnetic Wave (CMW) [12–14]. On the experimental front, collaborations such as STAR, PHENIX, and ALICE have presented evidence of CME and associated phenomena through the analysis of two-particle or three-particle correlations among charged particles relative to the reaction plane [15–20]. These findings exhibit a qualitative consistency with the CME and direct experimental affirmation for the existence of topologically non-trivial gluon configurations. Besides, these phenomena materialize at high colliding energy.

Additionally, some research groups conducted detail theoretical investigations into the generation of electromagnetic fields during HICs in the intermediate energy regime also. These findings meticulously explore the impact of diverse factors on the temporal and spatial evolution of electromagnetic fields. Recently, Dhanpat et al. [21,22] and X. G. Deng et al. [23] utilised the IQMD framework to get insights about the intricate correlation of various observables with the generation of magnetic field during HICs in different rapidity segments. In 2019, Y. Sun et al. [24] observed the effects of magnetic field on collective flow during HICs. Similarly, Li Ou [25] and Deng et al. [3] used the Isospin-dependent Boltzmann-Uhling-Uhlenbeck transport model (IBUU11) and HIJING theoretical framework, respectively to obtain profound understanding about the temporal and phase-space distribution of internal electromagnetic field.

* Corresponding author.
E-mail address: suneelkumar@cuh.ac.in (S. Kumar).

https://doi.org/10.1016/j.nuclphysa.2024.123005
Received 20 September 2024; Received in revised form 28 November 2024; Accepted 3 December 2024

Available online 6 December 2024

The dynamics of nucleons during HICs in the realm of intermediate energy regime is highly interesting due to the complex interplay between mean field potential and n-n scattering [26]. Within this energy regime, non-central HICs engenders the anisotropic form of pressure gradient [27,28] where several phenomena manifest themselves including multi-fragmentation, collective flow, nuclear stopping etc. [29–32]. This anisotropic pressure gradient influences the size and multiplicity of fragments [33–35]. The fragments have been classified according to their size and are distinctly identified as the free nucleons (FNs) [$A_f = 1$], light mass fragments (LMFs) [$2 \leq A_f \leq 4$], medium mass fragments (MMFs) [$5 \leq A_f \leq 9$] as well as intermediate mass fragments (IMFs) [$9 \leq A_f \leq 32$]. The meticulous investigation into the generation of magnetic fields by varied mass fragments in heavy ion collisions reveals a novel facet of the intricate dynamics, elucidating their distinct contributions.

To the best of our knowledge, the impact of different mass fragments on the generation of electromagnetic field during HICs in intermediate energy regime has not been extensively studied. Hence, this research endeavour seeks to fill this void by pursuing two main objectives:

- To study the contribution of different mass fragment in the generation of magnetic field
- Correlation of various observables with the generation of magnetic field for different mass fragments

2. Isospin quantum molecular dynamics

The Isospin-dependent Quantum Molecular Dynamics (IQMD) model [36,37] is highly sophisticated theoretical framework that enables the investigation of complex dynamics and interactions among nucleons across wide range of energy regimes, spanning from the low to high incident energies. The IQMD model exhibits remarkable prowess in accurately simulating diverse phenomena such as magnetic fields [21–23], multifragmentation [38,39], nuclear stopping [40], and collective flow [41], showcasing its versatility and effectiveness in capturing intricate nuclear dynamics in intermediate energy regime. This model comprises by three step framework. First and foremost, it is essential that the generation of the nuclei, termed as initialization. In this process, it is imperative to assign the co-ordinates $(\mathbf{r_i(t)}, \mathbf{p_i(t)})$ to the centres of Gaussian wave-packets. In co-ordinate space, nucleons are randomly distributed in the sphere of radius R $= R_o A^{1/3}$ (where A is the mass number). Likewise in momentum phase space, momenta of each nucleon is assigned in between 0 and Fermi momentum $(P_F(\mathbf{r_i}) = \sqrt{-\mathbf{2mU(r_i)}})$. The wave function corresponding to the i^{th} nucleon which has a mean position $\mathbf{r_i(t)}$ and mean momentum $\mathbf{p_i(t)}$ is expressed as:

$$f_i(\mathbf{r}, \mathbf{p}, t) = \frac{1}{\pi^3 \hbar^3} \, e^{-(\mathbf{r}-\mathbf{r_i}(t))^2 \frac{2}{L}} \, e^{-(\mathbf{p}-\mathbf{p_i}(t))^2 \frac{L}{2\hbar^2}}. \tag{1}$$

Where, the incorporation of system mass dependent Gaussian width (L) helps to achieve optimum nucleonic density profile for $^{197}_{79}$Au + $^{197}_{79}$Au system and its value is taken as 8.66 fm^2. After the initialization phase, the IQMD model regulates the acceleration of target and projectile nuclei towards each other, carefully ensuring the proper maintenance of centre-of-mass energy.

The IQMD model utilizes Hamiltonian equations of motion to precisely delineate the positions and momenta of all hadrons:

$$\frac{dr_i}{dt} = \frac{d\langle H \rangle}{dp_i} \; ; \; \frac{dp_i}{dt} = -\frac{d\langle H \rangle}{dr_i}, \tag{2}$$

where,

$$\begin{aligned} \langle H \rangle &= \langle T \rangle + \langle V \rangle \\ &= \sum_i \frac{p_i^2}{2m_i} + \sum_i \sum_{j>i} \int f_i(\mathbf{r}, \mathbf{p}, t) V_{ij}(\vec{r}', \vec{r}) \\ &\quad \times f_j(\mathbf{r}', \mathbf{p}', t) d\vec{r} d\vec{r}' d\vec{p} d\vec{p}'. \end{aligned} \tag{3}$$

$$\begin{aligned} V_{ij} &= V_{ij}^{Skyrme} + V_{ij}^{Yukawa} + V_{ij}^{Coul} + V_{ij}^{MDI} + V_{ij}^{Sym} \\ &= \left(t_1 \delta(\mathbf{r_i} - \mathbf{r_j}) + t_2 \delta(\mathbf{r_i} - \mathbf{r_j}) \rho^{\zeta-1} \left(\frac{\mathbf{r_i} + \mathbf{r_j}}{2} \right) \right) \\ &\quad + t_3 \frac{exp(|\mathbf{r_i} - \mathbf{r_j}|/\mu)}{(|\mathbf{r_i} - \mathbf{r_j}|/\mu)} + \frac{Z_i Z_j e^2}{|\mathbf{r_i} - \mathbf{r_j}|} \\ &\quad + t_4 \ln^2[t_5(\mathbf{p_i} - \mathbf{p_j})^2 + 1] \delta(\mathbf{r_i} - \mathbf{r_j}) \\ &\quad + t_6 \frac{1}{\varrho_0} T_{3i} T_{3j} \delta(\mathbf{r_i} - \mathbf{r_j}). \end{aligned} \tag{4}$$

The final step, referred to as nucleon-nucleon (n-n) collisions, occurs when two nucleons are considered to collide if the distance between their centroids is less than $\sqrt{\frac{\sigma_{tot}}{\pi}}$, these binary collisions between nucleons play a foremost role in interactions dynamics.

In this study, we have employed the MSTP algorithm (updated version of MST algorithm) to analyse the fragmentation as a secondary tool. MST method recognizes the nucleons belong to the same fragment if the spatial distance between their centroid is less than the 4 fm. Mathematically, this constraint can be expressed as:

$$r_i - r_j \leq 4fm \tag{5}$$

where r_i and r_j represents the nucleon's spatial coordinates. However, when two nuclei collide with high relative momentum resulting into unstable compound nuclei that leads its disintegration into different mass fragments. Herein, during early stage of reaction, nucleons with high relative momentum may seem close together in spatial space and form unstable fragments. But these fragments eventually disintegrate into FNs and LMFs. To overcome this issue, the MSTP method introduces an additional constraint on relative momentum of nucleons within the same fragment. This dual constraint ensures the early identification of more stable fragments, preventing the formation of loosely bound fragments. The constraint on the relative momentum expressed as:

$$p_i - p_j \leq p_{Fermi} \tag{6}$$

where p_i, p_j symbolize the momentum of i^{th} and j^{th}, and p_{Fermi} (260 MeV/c) is the Fermi momentum [42–44].

Analysing the evolution and influence of electromagnetic field on the moving charge particle, the integration of electromagnetic field is accomplished by introducing Lienard-Wiechert potentials [21,23,25].

$$e\vec{\boldsymbol{B}}(\vec{\boldsymbol{r}},t) = \frac{e^2}{4\pi\epsilon_0 c}\sum_n Z_n^{frag}\frac{c^2 - v_n^2}{\left(cR_n - \vec{\boldsymbol{R}}_n\cdot\vec{\boldsymbol{v}}_n\right)^3}(\vec{\boldsymbol{v}}_n \times \vec{\boldsymbol{R}}_n) \tag{7}$$

When $\boldsymbol{v}_n \ll$ c, the above equation turn into

$$e\vec{\boldsymbol{B}}(\vec{\boldsymbol{r}},t) = \frac{e^2}{4\pi\epsilon_0 c^2}\sum_n Z_n^{frag}\frac{1}{R_n^3}(\vec{\boldsymbol{v}}_n \times \vec{\boldsymbol{R}}_n) \tag{8}$$

where, Z_n^{frag} is the number of charge particle in n^{th} fragment, $\vec{\boldsymbol{R}}_n = \vec{\boldsymbol{r}} - \vec{\boldsymbol{r}}'_n$ is the relative position of the field point $\vec{\boldsymbol{r}}$ to the n^{th} particle's source point $\vec{\boldsymbol{r}}'_n$, and $\vec{\boldsymbol{v}}_n$ is the velocity of the n^{th} fragment at the retarded time $t_{rn} = t - \left|\vec{\boldsymbol{r}} - \vec{\boldsymbol{r}}'_n\left(t_{rn}\right)\right|/c$. It is imperative to note that the aforementioned equations have singularities when $R_n = 0$ approaches to zero. To tackle the difficulties posed by the singularities and self-interactions effect an organised approach is employed in which the particles residing in Lorentz-contracted cell are deliberately skipped from magnetic field calculations.

3. Results and discussion

In this work, the IQMD model framework has been integrated with MSTP algorithm to explore the complicated dynamics of heavy ion collisions in the intermediate energy regime. The detailed study of the production of magnetic field by the distinct mass fragments necessitates a thorough investigation on the some closely parameters that influences its strength. Strength of magnetic field is impacted by the multiplicity and the kinetic energy of charged fragments. Therefore, the variation of dN/dY vs $Y_{c.m.}/Y_{beam}$, dN/dE vs E_{ave}^{kin} and $dN/p_t dp_t$ vs p_t have been visualised to get insights about the multiplicity and kinetic energy of different mass fragments [44–50].

Fig. 1(a) illustrates the temporal evolution of the multiplicity of various mass fragments during $^{197}_{79}Au$ + $^{197}_{79}Au$ collisions at an incident energy of 80 MeV/nucleon with impact parameter range of b/b_{max} = 0.45 - 0.55. The multiplicity of all mass fragments increases over time, with a pronounced rise observed for FNs and LMFs compared to MMFs and IMFs. Likewise, Fig. 1(b) demonstrates the temporal evolution of multiplicity at higher colliding energy (400 MeV/nucleon), keeping all the other parameters same. Here, the multiplicity increase is more pronounced in the case of FNs and LMFs. Furthermore, Fig. 1(c) highlights the impact of colliding energy on FN's multiplicity. At higher energies, the multiplicity increases more rapidly due to a greater pressure gradient and enhanced energy transfer. The FN's multiplicity, shown in Fig. 1(c), exhibits a sharp rise at 400 MeV/nucleon, reflecting more energy transfer from participant matter to spectator matter. In contrast, at 80 MeV/nucleon, FN's multiplicity grows more gradually, indicating the dominance of the attractive mean field, which limits energy transfer. Moreover, Fig. 1(d) compares the IMF's multiplicity at 80 and 400 MeV/nucleon. At 400 MeV/nucleon, the IMF's multiplicity increases rapidly, attains maxima around 70 fm/c, and then declines due to the disintegration of IMFs into LMFs and FNs as a result of the substantial energy transfer. However, at 80 MeV/nucleon, the IMF's multiplicity remains relatively stable compared to higher incident energy and increases slowly over time. This stability is due to the less energy transfer at lower colliding energies, which limits significant fragmentation. These observations highlight the contrasting dynamics at low and high colliding energies. At lower colliding energy, interactions are dominated by attractive mean fields that suppress fragmentation while at higher colliding energies substantial transfer of energy takes place, driving more extensive fragmentation processes.

Furthermore, Fig. 2 demonstrates the correlation between dN/dY with scaled rapidity $Y_{c.m.}/Y_{beam}$ at different incident energy (80 and 400 MeV/nucleon), highlighting the unique characteristics of the production mechanism and source of nucleonic fragments in the various rapidity domains. Herein, the rapidity can be expressed as [51]:

$$Y(i) = \frac{1}{2}ln\frac{E(i) + p_z(i)c}{E(i) - p_z(i)c}. \tag{9}$$

Where, $p_z(i)$, $E(i)$ are the longitudinal momentum and total energy of the i^{th} nucleon and c is velocity of light. It has been observed from Fig. 2(a) that the dN/dY attains its maximum value at mid-rapidity region for all types of mass fragments. While going toward higher incident energy, 400 MeV/nucleon (Fig. 2(b)), two maxima at target and projectile rapidity have been obtained. Eventually,

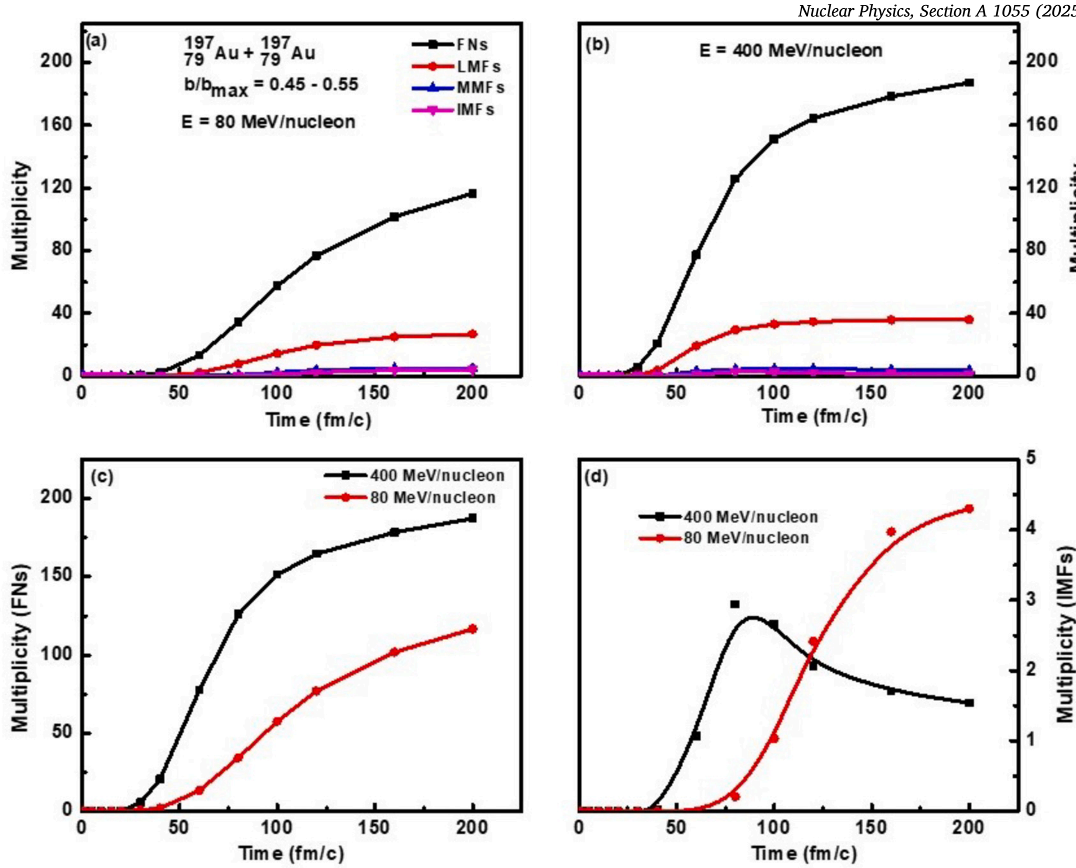

Fig. 1. Time evolution of multiplicity of different mass fragments at colliding energy of (a) 80 MeV/nucleon; (b) 400 MeV/nucleon; (c) comparison of FNs multiplicity at 80 MeV/nucleon and 400 MeV/nucleons; (d) comparison of IMFs multiplicity at 80 MeV/nucleons and 400 MeV/nucleons, at b/b_{max} = 0.45 - 0.55 for ${}^{197}_{79}Au$ + ${}^{197}_{79}Au$ collision.

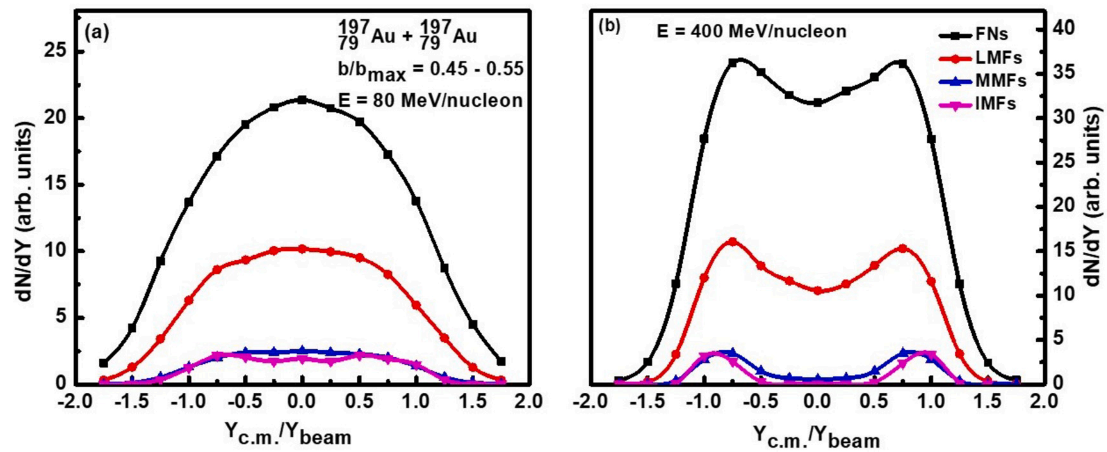

Fig. 2. The rapidity distribution (dN/dY) as a function of scaled rapidity (= $Y_{c.m.}/Y_{beam}$) for different mass fragments at (a) 80 MeV/nucleon (b) 400 MeV/nucleon within the impact parameter (b/b_{max}) range of 0.45 - 0.55.

from the Fig. 2 one can also conclude that the fragments have higher multiplicity at 400 MeV/nucleon, in comparison to 80 MeV/nucleon. This phenomenon is attributed to the more transfer of energy takes place from participant to spectator at incident energy of 400 MeV/nucleon, thereby the fragments are very excited and unbounded at higher incident energy. Moreover, it also provides insights into the intricate origin of different mass fragments such as FNs and LMFs originating from a complete stopped source. Whereas, MMFs and IMFs originate from the target and projectile rapidity.

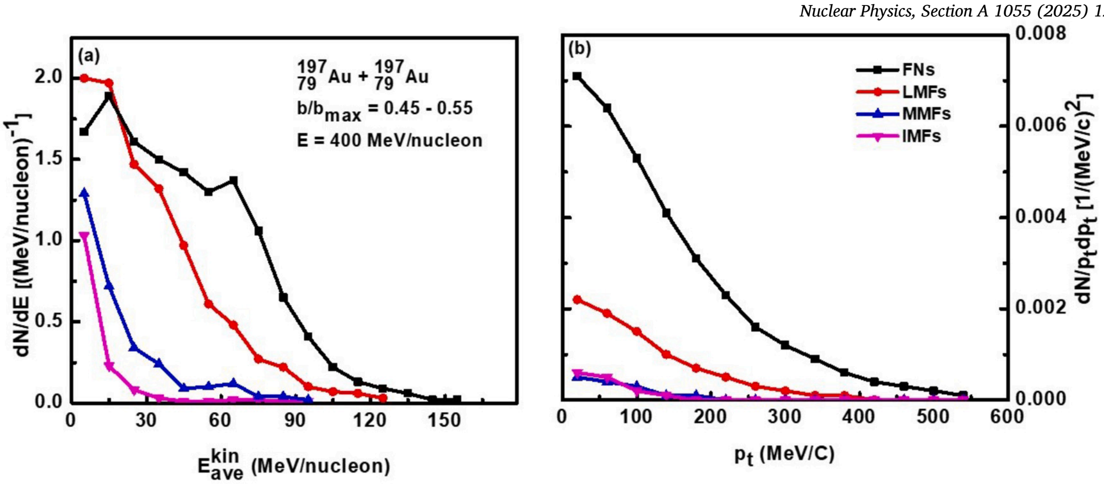

Fig. 3. (a) Variation of kinetic energy spectra (dN/dE) with E_{ave}^{kin} (b) variation of $dN/p_t dp_t$ $(1/(MeV/c)^2)$ as a function of the transverse momentum p_t for different mass fragments at 400 MeV/nucleon for impact parameter (b/b_{max}) = 0.45 - 0.55.

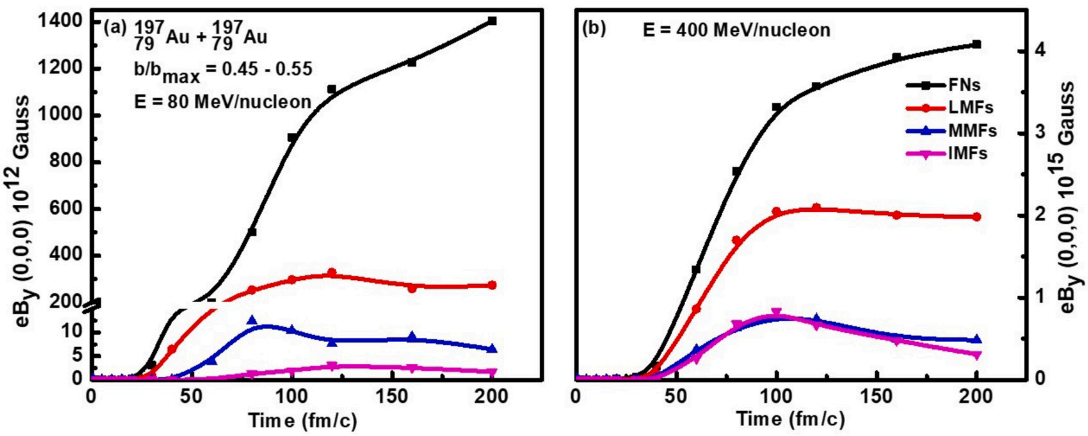

Fig. 4. (a) Time evolution of $eB_y(0,0,0)$ for different mass fragments (FNs, LCPs, IMFs and MMFs) at b/b_{max} = 0.45 - 0.55 for incident energy (a) 80 MeV/nucleon and (b) 400 MeV/nucleon.

To further deepen the study on multi-fragmentation, the evaluation of kinetic energy spectra of fragmentation in $^{197}_{79}Au + ^{197}_{79}Au$ collision is very interesting. Therefore, Fig. 3(a) depicts the nucleon spectra as a function of kinetic energy for different mass fragments. It has been observed that FNs have more kinetic energy, in comparison to heavier mass fragments. Likewise, the Fig. 3(b) depict the variation of $dN/p_t dp_t$ vs p_t that adds the nuance dimension in the understanding the behaviour of different mass fragments. It has been observed that the FNs and LMFs display sharp decrease in $dN/p_t dp_t$, as compared to MMFs and IMFs.

Interestingly, these fragments play a crucial role in the production of magnetic field during HICs. Within a time frame of 30 fm/c, a substantial compression region is generated during the initial stage of collision. Subsequently, energy is transferred from the participant to spectator matter resulting into the production of varying mass fragments. These fragments have significant contribution in the production of magnetic fields with varying intensity due to their distinct kinetic energy. Therefore, Fig. 4 demonstrates the time evolution of magnetic field at 80 and 400 MeV/nucleon for various kinds of mass fragments. It can be clearly observed from the Fig. 4 that the magnetic field generated by the FNs and LCPs is considerably more pronounced than that produced by MMFs and IMFs, due to considerably high kinetic energy of FNs and LMFs. Furthermore, it is noteworthy to mention that magnetic field intensity reaches its peak value around 100 fm/c for MMFs and IMFs, then starts decreasing slowly. But, it gets almost saturated for the LMFs while it increases progressively for the FNs. This might be attributed to the fact that as the time evolves, multiplicity of IMFs and MMFs starts decreasing while for FNs and LMFs, it increases subsequently. Moreover, the behaviour of magnetic field production by different mass fragments is almost similar at both incident energy (80 and 400 MeV/nucleon), but the intensity of magnetic field enhances remarkably in case of higher incident energy (shown in Fig. 4b). Likewise, the influence of impact parameter on the intensity of magnetic field generated by various mass fragments has been demonstrated in Fig. 5. It clearly reflects that the intensity decreases continuously for the FNs, attributing to the decrease in multiplicity with increase in the impact parameter. While for all other fragments, the intensity gets maximum near to semi-central collision and then decreases continuously.

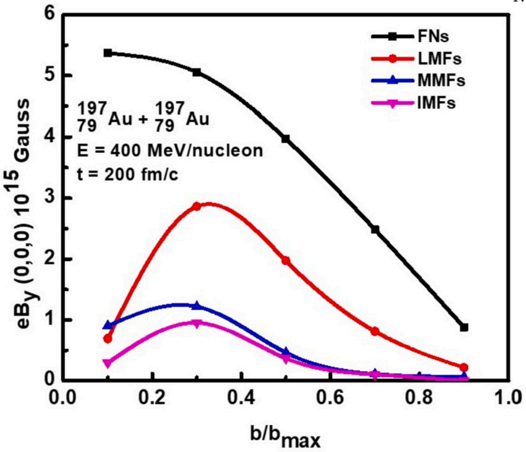

Fig. 5. Variation of $eB_y(0,0,0)$ with scaled impact parameter for different mass fragments at 400 MeV/nucleon.

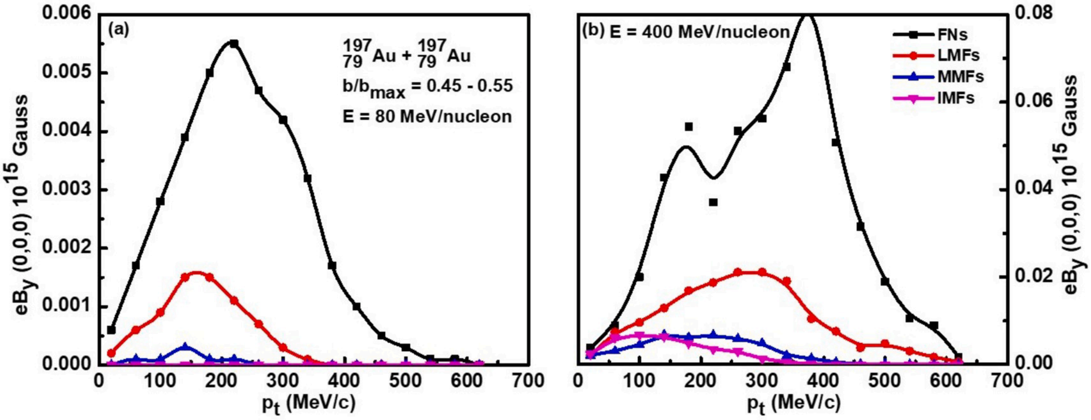

Fig. 6. Variation of $eB_y(0,0,0)$ with transverse momentum (p_t) for different mass fragments (FNs, LCPs, IMFs and MMFs) at incident energy of (a) 80 MeV/nucleon and (b) 400 MeV/nucleon at b/b_{max} = 0.45 - 0.55.

Furthermore, it is also imperative to encompass more comprehensive insights about the variation of the magnetic field intensity due to different mass fragments in relation to their transverse momentum. As we progress towards higher transverse momentum, the magnetic field intensity reaches its maximum and subsequently undergoes gradual decrease for FNs and LMFs at 80 MeV/nucleon incident energy (shown in Fig. 6a). And the contribution from MMFs and IMFs is almost negligible in the generation of magnetic field. Likewise, Fig. 6(b) demonstrates the variation of magnetic field intensity with transverse momentum for different mass fragments at higher incident energy (400 MeV/nucleon). It is worth mentioning that the strength of magnetic field increases at higher colliding energy. The magnetic field intensity for the FNs and LMFs is significantly higher within a specific range of transverse momentum. While the intensity of magnetic field reduced remarkably for the MMFs and IMFs owing to their lesser kinetic energy. Interestingly, the maxima of magnetic field intensity shift towards lower transverse momentum going towards heavier mass fragments. This is ascribed to the fact that IMFs and MMFs originate from the spectator region resulting into higher in-plane momentum. Hence, IMFs and MMFs exhibit less value of transverse momentum and therefore, maxima of their magnetic field intensity lies at lower side of transverse momentum.

Eventually, a kinetic variable “rapidity” which is closely related to the velocity of particles, and therefore, the study of magnetic field variation with rapidity provides valuable information about the features of the produced fragments and the underlying physics behind the generation of magnetic field in different rapidity segments. Therefore, Fig. 7 reflect the variation of magnetic field intensity with the rapidity for different mass fragments. Fig. 7(a) depicts that the intensity of magnetic field approaches to zero in the near zero-rapidity zone. This is attributed to the fact that the nuclear stopping experienced by FNs and LCPs is extremely high resulting into high energy loss. While the multiplicity of MMFs and IMFs in this rapidity zone is negligible, therefore their contribution to the generation of magnetic field is also negligible in this range. Further, going apart from the mid-rapidity zone, the intensity of magnetic field intensity rises sharply to reach its maximum and then decreases. This is due to lesser nuclear stopping experienced by the fragments as well as more in-plane momentum and thus, contributes in the generation of magnetic field. Noticeably, the magnetic field intensity is highest for the FNs and LCPs as compared to MMFs & IMFs, reason being higher kinetic energy as discussed in Fig. 3.

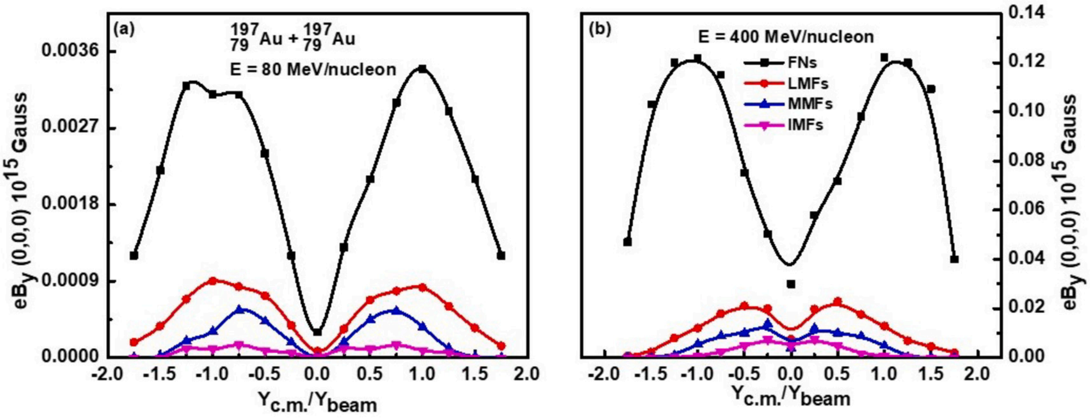

Fig. 7. Variation of $eB_y(0,0,0)$ with scaled rapidity ($Y_{c.m.}/Y_{beam}$) for different mass fragments (FNs, LCPs, IMFs and MMFs) at incident energy of (a) 80 MeV/nucleon and (b) 400 MeV/nucleon at b/b_{max} = 0.45 - 0.55.

Moreover, the Fig. 7(b) demonstrates the similar pattern with higher strength of magnetic field has been observed at higher colliding energy (400 MeV/nucleon).

4. Summary

Conclusively, the IQMD model has been utilised as the primary tool for generating phase space while the MSTP algorithm integrated as the secondary tool for clusterization. The temporal evolution of the magnetic field induced by distinct mass fragments elucidated that the contributions from FNs and LMFs was remarkably higher compared to heavier mass fragments (MMFs and IMFs). When moving towards higher centrality, the contribution of FNs decreases continuously while other higher mass fragments exhibit a peak around the semi-central impact parameter before decreasing. Further elaboration on the magnetic field for different mass fragments with respect to transverse momentum and the rapidity distributions revealed compelling outcomes. The dip near zero-rapidity for FNs was attributed to increased nuclear stopping. Conversely, this dip occurs due to a reduced number of fragments near zero-rapidity for heavier mass fragments. Moving towards target and projectile rapidity regimes, nuclear stopping diminished which consequently enhances the acceleration of charged particles resulting into heightened magnetic field intensity. This comprehensive analysis enriches our understanding about the contribution of different mass fragments in the production of magnetic field during heavy ion collisions.

CRediT authorship contribution statement

Dhanpat Sharma: Writing – review & editing, Writing – original draft, Visualization, Validation, Methodology, Investigation, Formal analysis, Data curation, Conceptualization. **Suneel Kumar:** Writing – review & editing, Visualization, Validation, Supervision, Software, Resources, Conceptualization.

Declaration of competing interest

The authors declare that they have no known competing financial interests or personal relationships that could have appeared to influence the work reported in this paper.

Acknowledgement

The authors would like to thank Prof. R. K. Puri for his insightful discussion and for providing access to the computer programs used in this work. One author, Dhanpat Sharma thankful to UGC-CSIR (Reference No.- 1474/(CSIR-UGC NET JUNE 2019)) for providing senior research fellowship (SRF).

Data availability

Data will be made available on request.

References

[1] G. Inghirami, et al., Eur. Phys. J. C 80 (3) (2020) 293.
[2] C. Gale, et al., Phys. Rev. C 105 (1) (2022) 014909.
[3] W.T. Deng, et al., Phys. Rev. C 85 (4) (2012) 044907.

[4] V. Voronyuk, et al., Phys. Rev. C 83 (5) (2011) 054911.
[5] J. Liao, Nucl. Phys. A 956 (2016) 99–106.
[6] D.E. Kharzeev, D.T. Son, Phys. Rev. Lett. 106 (6) (2011) 062301.
[7] S. Choudhury, et al., Chin. Phys. C 46 (1) (2022) 014101.
[8] D.E. Kharzeev, J. Liao, Nat. Rev. Phys. 3 (1) (2021) 55–63.
[9] R. Belmont, J.L. Nagle, Phys. Rev. C 96 (2) (2017) 024901.
[10] D.E. Kharzeev, Phys. Lett. B 633 (2006) 260.
[11] A. Flachi, K. Fukushima, Phys. Rev. D 98 (2018) 096011.
[12] Y. Burnier, et al., Phys. Rev. Lett. 107 (5) (2011) 052303.
[13] D.E. Kharzeev, H.U. Yee, Phys. Rev. D 83 (2011) 085007.
[14] H.J. Xu, et al., Phys. Rev. C 101 (2020) 014913.
[15] B.I. Abelev, et al., STAR Collaboration, Phys. Rev. Lett. 103 (2009) 251601.
[16] B.I. Abelev, et al., STAR Collaboration, Phys. Rev. C 81 (2010) 054908.
[17] N.N. Ajitanand, et al., PHENIX Collaboration, Proc. RBRC Workshops 96 (2010).
[18] N.N. Ajitanand, et al., Phys. Rev. C 83 (1) (2011) 011901.
[19] B.I. Abelev, et al., Phys. Rev. Lett. 110 (11) (2013) 012301.
[20] Y. Zhong, et al., Adv. High Energy Phys. 2014 (2014).
[21] D. Sharma, S. Kumar, J. Phys. G, Nucl. Part. Phys. 50 (4) (2023) 045109.
[22] D. Sharma, S. Kumar, J. Phys. G, Nucl. Part. Phys. 51 (5) (2024) 055102.
[23] X.G. Deng, Y.G. Ma, Phys. Rev. C 101 (5) (2020) 054610.
[24] Yet Sun, et al., Phys. Rev. C 99 (6) (2019) 064607.
[25] L. Ou, B.A. Li, Phys. Rev. C 84 (6) (2011) 064605.
[26] B. Gao, et al., Phys. Lett. B 838 (2023) 137685.
[27] S. Voloshin, Y.J. Zhang, Phys. Rev. C 70 (1996) 665.
[28] H. Appelshauser, et al., NA49 Collaboration, Phys. Rev. Lett. 80 (1998) 4136.
[29] Pet Bansal, et al., Eur. Phys. J. A 51 (11) (2015) 139.
[30] L. Li, F.Y. Wang, Y.X. Zhang, Nucl. Sci. Tech. 33 (5) (2022) 58.
[31] A. Ono, Prog. Part. Nucl. Phys. 105 (2019) 139–179.
[32] P. Napolitani, M. Colonna, Phys. Lett. B 797 (2019) 134833.
[33] S. Kumar, S. Kumar, R.K. Puri, Phys. Rev. C 78 (6) (2008) 064602.
[34] S. Kumar, S. Kumar, R.K. Puri, Phys. Rev. C 81 (1) (2010) 014601.
[35] S. Goyal, R.K. Puri, Phys. Rev. C 83 (4) (2011) 047601.
[36] C. Hartnack, et al., Eur. Phys. J. A 1 (151) (1998).
[37] C. Hartnack, et al., Phys. Rep. 510 (2012) 119.
[38] N.K. Dhillon, et al., Eur. Phys. J. A 58 (1) (2022) 7.
[39] R. Rana, et al., Braz. J. Phys. 53 (5) (2023) 132.
[40] R. Rana, et al., Eur. Phys. J. A 59 (6) (2023) 137.
[41] L.M. Fang, et al., Phys. Rev. C 107 (4) (2023) 044904.
[42] S. Kumar, et al., Phys. Rev. C 58 (1) (1998) 320–345.
[43] S. Sood, et al., Phys. Rev. C 99 (2019) 054612.
[44] J. Singh, et al., Phys. Rev. C 63 (5) (2001) 054603.
[45] S. Kumar, et al., Phys. Rev. C 60 (5) (1999) 054607.
[46] S. Gautam, et al., Ukr. J. Phys. 57 (6) (2012) 599–605.
[47] S. Kumar, et al., Phys. Rev. C 78 (6) (2008) 064602.
[48] S. Kumar, et al., Phys. Rev. C 84 (4) (2011) 044620.
[49] R.K. Puri, et al., Pramana 59 (2002) 19–31.
[50] J.K. Dhawan, R.K. Puri, Phys. Rev. C 74 (5) (2006) 054610.
[51] J. Aichelin, Phys. Rep. 202 (1991) 233.